Multiferroism in strained strontium hexaferrite epitaxial thin films

Joonhyuk Lee, Sam Yeon Cho, Inhwan Kim, Christopher M. Rouleau, Kungwan Kang, Sangkyun Ryu, Yunseok Heo, Jong K. Keum, Daniel M. Pajerowski, Younghak Kim, Sang Don Bu, Jaekwang Lee, and Hyoungjeen Jeen

Phys. Rev. Materials **8**, 024401 — Published 5 February 2024
DOI: 10.1103/PhysRevMaterials.8.024401

Multiferroism in strained strontium hexaferrite epitaxial thin films

Joonhyuk Lee[1,#], *Sam Yeon Cho*[2,#], *Inhwan Kim*[1,#], *Christopher M. Rouleau*[3], *Kungwan Kang*[1], *Sangkyun Ryu*[1], *Yunseok Heo*[1], *Jong K. Keum*[3], *Daniel M. Pajerowski*[4], *Younghak Kim*[5], *Sang Don Bu*[2,*], *Jaekwang Lee*[1,*], *Hyoungjeen Jeen*[1,*]

[1]*Department of Physics, Pusan National University, Busan 46241, South Korea*

[2]*Department of Physics, Jeonbuk National University, Jeonju 54896, South Korea*

[3] *Center for Nanophase Materials Sciences, Oak Ridge National Laboratory Oak Ridge, TN 37831, USA*

[4]*Neutron Scattering Division Oak Ridge National Laboratory Oak Ridge, TN 37830, USA*

[5]*Pohang Accelerator Laboratory, POSTECH, Pohang, 37673, South Korea*

ABSTRACT

Ferrimagnetic $SrFe_{12}O_{19}$ (SrM) is a mother phase for ferrite permanent magnets, which are commonly used due to its low cost compared to that of Nd-based permanent magnets and broader uses in permanent magnet markets. Recently, it has been debated its electronic ground state. It has been proposed, in its single crystal form, the SrM is in a quantum paraelectric state, while polycrystalline SrM is a ferroelectric state. In this work, strain can stabilize ferroelectricity at room temperature, while keeping its ferrimagnetism. The strained SrM shows not only clear magnetic hysteresis but also ~ 4.4 μC/cm^2 as remnant polarization. From high temperature thermal annealing, its crystallinity and ferroelectricity are even strengthened. Those are visualized by significant reduction in full width half maximum of the rocking curve and ~ 7.9 μC/cm^2 in remnant polarization The results indicate the new functionality can be discovered from old and well-known materials.

Hexaferrites have served as the backbone for ferrite permanent magnets[1,2]. Its lower cost compared to that of Nd-based magnet has made it popular in this sector of the markets. However, their intrinsically low saturation magnetization has always been considered to be improved. To improve their magnetic properties, industrial approaches have been based on ‘alchemy’ based routes, which involve random substitution of elements such as Co, La, and Ba.[1,2] Industrial needs are primarily focused on the use of cost-effective elements, but until recently, the structure-property relationships has not been actively considered in this material. For example, since the magnetic ground state of most hexaferrites is ferrimagnetic (See. Fig. 1), it should be possible to tune the magnetic exchange interaction through structural modifications from strain engineering[3-5].

Recently, hexaferrites have attracted attentions due to their possible multifunctionality. For example, several hexaferrites were discovered to have multiferroic property.[6-9] However, in *M*-type hexaferrite $SrFe_{12}O_{19}$ (SrM), the electronic ground state is still controversial.[10-12] Rowley *et al.* argued that due to quantum criticality, their ferroelectric Curie temperature should occur at cryogenic temperatures. In their work, they claimed that the uniaxial electric dipole moment along the *c*-axis was due to off-equator displacements of Fe^{3+} in the FeO_5 lattice (See Fig. 1). However, quantum fluctuations prevent the onset of long-range ferroelectric ordering. However, Kostishyn *et al.* observed clear room temperature ferroelectric hysteresis with ~ 45 $\mu C/cm^2$, which supports multiferroism in this material[13]. In addition, Tan *et al.* claimed oxygen treatment at moderate temperature enhanced its polarization value over 100 $\mu C/cm^2$ at room temperature[12].

Given these observations, it is reasonable to assume that epitaxial strain may induce similar lattice distortions in SrM to promote ferroelectricity as strain is known to be an active knob to perturb the electronic properties of perovskite-based complex oxides[14-17], for example.

In this work, we stabilized epitaxial (001) $SrFe_{12}O_{19}$ on (111) $SrTiO_3$ and observed robust ferroelectricity at room temperature. Due to the intrinsic difference in lattice constants between the film and the substrate, the films include a built-in substrate-induced strain. From density functional theory, strain can stabilize ferroelectricity through off-centering of Fe ions. Thus, we conclude the $SrFe_{12}O_{19}$ epitaxial film is multiferroic.

(001) $SrFe_{12}O_{19}$ (SrM) on (111) $SrTiO_3$ (STO) or (111) Nb-doped STO (0.5% Nb doping) were grown by pulsed laser deposition (PLD). To optimize the growth conditions, each film was grown at temperatures ranging from 650 to 800°C, oxygen partial pressures ranging from 0.005 mTorr to 100 mTorr, a laser of 2.2 mJ/cm^2, and a repetition rate of 10 Hz. A KrF excimer laser with a wavelength of 248 nm was used. The as-deposited films were cooled in the same growth oxygen partial pressure in which they were grown. The impurity-free and epitaxial films grown under optimal conditions (800°C, 10 mTorr) were post-annealed in air to enhance their crystallinity.

For structural analysis, all the films were characterized with x-ray reflectivity, θ-2θ scan, and ω rocking curves. Several samples were analyzed with φ-scans to find the epitaxial relationship between the SrM film and STO substrate. Surface morphologies were also checked with atomic force microscope, particularly potential surface roughening due to high temperature thermal annealing and we found no significant surface roughening occurred in our SrM.

To determine valence state and metal-oxygen hybridization, X-ray absorption spectroscopy (XAS) of the Fe *L*-edge and O *K*-edge and X-ray magnetic circular dichroism (XMCD) were performed using the 2A beamline at the Pohang accelerator laboratory. Elemental specific- and bulk- magnetism were determined using the XMCD and a SQUID magnetometer (MPMS-3 from Quantum Design). Since SrM has strong crystalline magnetic anisotropy[18,19], all the magnetic information is from the out-of-plane direction, which is equivalent to the surface normal of the thin film. Sum rule was applied to find element-specific spin magnetic moment (M_{spin})and orbital magnetic moment (M_{orbital}). Details can be found in the previous works[20-22]. To determine potential multiferrism in SrM, ferroelectric test and dielectric measurements were performed at room temperature. Dynamic hysteresis measurement technique was applied for the P-E loops and I-E curves with TF analyzer 2000 from AixACCT Co.

Theoretical calculations were performed using the first-principles density functional theory with the plane-wave-based Vienna *ab initio* simulation package (VASP) [23-25]. The revised Perdew, Burke, and Ernzerhof generalized gradient approximation is adpated for the exchange-correlation function [26]. We use the projector augmented wave (PAW) potentials that include ten valence electrons for Sr ($4s^2$, $4p^6$, and $5s^2$) atom, eight for Fe ($3d^7$ and $4s^1$) atom, and six for O ($2s^2$ and $2p^4$) atom [27]. The unit cell in our calculations has two Sr atoms, twenty four Fe atoms, and thirty eight O atoms with the optimized lattice parameter of $a = b = 5.855$ Å, and $c = 22.831$ Å. A plane-wave cutoff energy of 600 eV is used with a Monkhorst-Pack grid with 8×8×2 k-point mesh is used for the all calculations[28]. We use the nudged elastic band (NEB) method to calculate the ferroelectric double well potential energy barrier [29]. We applied the onsite Hubbard-U correction of 4 eV to Fe using the Dudarev formalism [30]. We have considered the ferrimagnetic collinear spin ordering on the Fe atoms consisting of the up spin on the two bipyramidal and fourteen octahedral Fe sites whereas the down spin on the four octahedral and the two tetrahedral Fe sites, respectively. All calculations are converged in energy to 10^{-7} eV per unit cell and the structures are fully optimized with the forces convergence of 10^{-3} eV/Å.

Growth condition optimization is based on structural characterization of the as-grown SrM thin films. Growth PO_2 and growth temperature (T_S) were used as parameters to optimize the epitaxial SrM thin films. Figure 2(a) shows single crystal epitaxial thin films are obtained in relatively narrow growth conditions, where the T_S is at 800°C and PO_2 is between 1 and 10 mTorr.

Figures 2(b), (c), and (d) show x-ray reflectivity (XRR), θ-2θ scan, and φ-scans from the *c*-axis oriented optimized thin film. XRR shows clear Kiessig fringes, and the thickness of the as-grown film was determined to be ~ 70 nm. Figure 2(c) shows the normal scan of the optimized SrM films, and it is clearly seen that the film is epitaxial and *c*-axis oriented without any impurities. The result is consistent with the previous report[31]. To elucidate the epitaxial relationship between SrM and STO, we performed φ-scans of $(20\underline{13})$ SrM and (220) STO, respectively. The results from (220) STO shows three-fold symmetry, while those from $(20\underline{13})$ SrM shows six-fold symmetry. In addition, the peak positions from the STO and the SrM coincid. Confirming the heteroepitaxial growth of SrM thin films on 111 STO substrates with a $(0001)[11\bar{2}0]$ SrM // (111) $[1\bar{1}0]$ STO.

Although the SrM thin films were epitaxial, the full width half maximum (FWHM) from the rocking curve result of the as-grown SrM was ~0.7°, which is rather broad. In order to enhance the crystallinity of the SrM film, we post-annealed several SrM samples in air using a muffle furnace. Figure 3(a) shows that with thermal annealing, the rocking curve peak is shapened, while the cyrstallinity did not deterioate. Figure 3(b) shows the $00\underline{14}$ rocking curves. The FWHM value was reached down to ~0.15°, when the film was annealed at 1100°C. When we compared AFM images between the as-grown SrM and the annealed SrM at 1100°C, the r.m.s. roughness (~1 nm) was essentially unchanged. Figure 3(c) and (d) show that the grain growth occurs, and as a result we can claim that growth aggromoration in addition to enhanced crystallinity occured. Note that we also observed the enhanced contrast in Kiessig fringes in x-ray reflectivity (See Figure 3(e)).

After confirming considerable changes in crystallinity in the annealed SrM, XAS was used to determine the valence state of Fe and metal-oxygen hybridization. XAS data from the Fe *L*-edge show the valence states of both the as-grown and th e annealed SrMs are nearly identical.

Especially, the L_2-edge spectrum consists of doublet, where each peak is closedly related to the number of electrons in either t_{2g} and e_g levels in Fe ions[32]. The similar shape in the L_2-edge specra indicates valence state are not changed as shown in Figure 4(a). From these results, the valence state of Fe ions in both SrMs is 3+. Thermal annealing does not lead changes in valence, but only crystallinity. XAS data from the O *K*-edge were also obtained to see the changes in metal-oxygen hybridization. Both spectra near 532 eV show double peak features, which are originate from crystal field splitting between t_{2g} and e_g sites [33]. Although we observed a slight increase of peak intensity near 532 eV, corresponding to Fe-O hybridization, overall the spectra are similar and indicate enhanced crystallinity does not lead to the dramatic changes in chemical state.

XMCD measurements were performed at room temperature in a 0.5 T magnetic field as shown in Fig. 4(c). The XMCD features are qualitatively similar to that of previously reported results.[33] Note that we clearly observed two dips and two peaks. The two dips are the magnetic signal originating from octahedral irons, while the peak are the magnetic signal originating from tetrahedral irons[33]. These are alighned antiferromagnetically. As can be seen from Fig. 4(d), the coercive fields in our SrM films are less 0.3 T and therefore XMCD in 0.5 T will reflect a magnetically saturated state. In both the SQUID and XMCD data, the saturated magnetic moment of the annealed SrM film is higher than that of the as-grown SrM film. Quantitatively, from M vs. H curves, we calculated saturation magnetic moment in Bohr magneton per Fe. The values are 1.02 μ_B/Fe for as-grown SrM and 1.26 μ_B/Fe. When we adopted the sum rule [20,21] and calculated element-specific spin magnetic moment (M_{spin}) and orbital magnetic moment (M_{orbital}) from Fe *L*-edge XMCD. As seen in Table R1, the M_{spin} from the annealed SrM is larger than that from the as-grown SrM film, while the M_{orbital} shows that the magnitude of the M_{orbital} is larger from the as-grown SrM. Since the M_{spin} and M_{orbital} are contributed in opposite way, the difference in overall magnetic moment from Fe *L*-edge XMCD spectra is further apart. The overall value is slightly smaller than that from the saturation magnetic moment, thus we believe magnetism is mainly form the Fe sites and their interactions.

To check whether our SrM are ferroelectric, we measured dielectric constants and polarization-electric field (*P*-*E*) at room temperature. For realizing capacitor geometry, we grew SrM thin films on 0.5% Nb doped $SrTiO_3$. With the Pt top electrode, we could form the capacitor geometry for the measurements of electrical properties. (We here note that such an asymmetric electrode strucure can result in an asymmetry in the shape of hysteresis loop such as imprint.) First Fig. 5(a) and (b) show frequency-dependence on dielectric constants and dissipation factors of as-grown and annealed thin films, respectively, from the multiple points in each film. As can be seen that both dielectric constant (ε) and dissipation factor ($\tan(\delta)$) are well-matched. This indicates spatially uniform dielectric properties in each film. In addition, the dielectric constants are around 400 and 600 at 10^4 Hz for as-grown and annealed thin films, respectively, which are similar to those of SrM ceramics [12] and the small values (>1) of dissipation fatctors suggest that the films has a high quality with low dielectric loss. Note that overall dielectric constant from the annealed SrM shows higher that that of the as-grown SrM.

Next, Figs. 5(c) through (f) are *P*-*E* and current vs. electic field (*I*-*E*) curves of each film. Even though each curve shows an asymmetric shape as expected, distinct ferroelectric hysteresis curves were obtained for SrM thin films with driving voltages of up to 300 kV/cm. The increases in the remanant polarization (P_r) and the coercive field (E_c) with the driving voltage confirm that the SrM exhibit significant ferroelectric properties. The P_r of the as-grown SrM is thus estimated to be ~4.4 μC/cm^2, while the P_r of the annealed SrM is ~7.9 μC/cm^2. In addition, the annealed SrM has the lower E_c value of 91 kV/cm than that of as-grown film (144 kV/cm). More importantly, in the *I*-*E* curves, it is clearly seen current peaks. This indicate direct displacement current peaks, which imply the presence of spontaneous polarization (P_s) switching. These show that our SrM films have some typical ferroelectric behavior [34]. Even if both as-grown and the annealed SrMs are ferroelectric, the annealed SrM has the higher remnant polarization (P_r). In I-E curves in Figs. 5(e) and (f), rather broader peaks and dips near the zero field can be seen. It is likely that the broader peak and dip near zero bias are found in Mn and/or Fe-based multiferroic materials such as $CoFe_2O_4$-doped $_{0.94}Na_{0.5}Bi_{0.5}TiO_3$-$_{0.06}BaTiO_3$ and YMO_3. This is related to modulation in space charge polarization due to the fluctuation of transition metal's valence state[35,36].

To elucidate the physical origin of the ferroelectric behavior in ferrimagnetic strained SrM, we apply the biaxial compressive strain along the in-plane direction. As shown in Fig. 6(a), the energy difference between ferroelectic and paraelectric phase always shows negative value, supporting that the ferroelectric state is energetically favorable under the biaxial compressive strain. We can see that the compressive biaxial strain generates the ferroelectric atomic displacements in paraelectric SrM and induces the phase transition to ferroelectric SrM. (See the inset of Fig. 6(a)). Figure 6 (b) shows the double well potential for the 3% strained SrM. The energy barrier is estimated about 0.03 eV per each formula unit, and the value of the electric polarization is 5 $\mu C/cm^2$. Interestingly, even if Fe ions are distributed in bipyramidal, octaheral, and tetrahedral sites, the ferroelectric atomic displacements have been induced only at the bipyramid sites. Such a selective response is unique in SrM and quite different from substrate-induced ferroelectricity observed in conventional ferroelectric complex oxides [15,37-39].

In summary, we stabilized epitaxial (001) $SrFe_{12}O_{19}$ on (111) $SrTiO_3$ and observed robust ferroelectricity at room temperature. In addition, thermal annealing strengthens both ferroelectricity and magnetism by enhancing crystallinity. The stabilization of ferroelectricity under compressive strain is likely due to off-centering of Fe ions from DFT calculation. Since both ferrimagnetism and ferroelectricity are from the same element, it is expected a large magnetoelectric coupling[12] and its tuning by control of strain state.

ACKNOWLEDGEMENTS

This work was supported by National Research Foundation of Korea (NRF-2018M2A2B3A01071859). PLD and XRD were conducted as part of a user project at the Center for Nanoscale Materials Sciences (CNMS), which is a U.S. Department of Energy, Office of Science User Facility at Oak Ridge National Laboratory. Partly, this work was financially supported by the 2022 Post-Doc. Development Program of Pusan National University. DFT calculation and XRD measurements were supported by Korea Basic Science Institute (National research Facilities and Equipment Center) grant funded by the Ministry of Education.(2021R1A6C101A429). JL, SYC, and IK are equally contributed in this work.

References

[1] C. de Julián Fernández, C. Sangregorio, J. de la Figuera, B. Belec, D. Makovec *et al.*, J. Phys. D: Appl. Phys. **54**, 153001 (2021).

[2] R. C. Pullar, Prog. Mater Sci. **57**, 1191 (2012).

[3] S. Shinde, R. Ramesh, S. Lofland, S. Bhagat, S. Ogale *et al.*, Appl. Phys. Lett. **72**, 3443 (1998).

[4] Q. Zhu, R. Tang, F. Peng, S. Xu, G. Liang *et al.*, Physical Review Applied **16**, 054006 (2021).

[5] C. Ederer and N. A. Spaldin, Phys. Rev. B **71**, 224103 (2005).

[6] S. Trukhanov, A. Trukhanov, M. Salem, E. Trukhanova, L. Panina *et al.*, Ceramics International **44**, 21295 (2018).

[7] S. Trukhanov, A. Trukhanov, V. Kostishyn, L. Panina, A. V. Trukhanov *et al.*, Journal of Magnetism and Magnetic Materials **442**, 300 (2017).

[8] Y. S. Chai, S. H. Chun, J. Z. Cong, and K. H. Kim, Phys. Rev. B **98**, 104416 (2018).

[9] G. Tan and X. Chen, J. Magn. Magn. Mater. **327**, 87 (2013).

[10] S. E. Rowley, Y.-S. Chai, S.-P. Shen, Y. Sun, A. T. Jones *et al.*, Sci. Rep. **6**, 25724 (2016).

[11] V. G. Kostishyn, L. V. Panina, A. V. Timofeev, L. V. Kozhitov, A. N. Kovalev *et al.*, J.

Magn. Magn. Mater. **400**, 327 (2016).

[12] G. Tan and H. Sheng, PLoS ONE **11**, e0167084 (2016).

[13] V. Kostishyn, L. Panina, A. Timofeev, L. Kozhitov, A. Kovalev *et al.*, Journal of Magnetism and Magnetic Materials **400**, 327 (2016).

[14] A. Biswas, M. Rajeswari, R. C. Srivastava, Y. H. Li, T. Venkatesan *et al.*, Phys. Rev. B **61**, 9665 (2000).

[15] K. H. Ahn, T. Lookman, and A. R. Bishop, Nature **428**, 401 (2004).

[16] A. J. Hatt and N. A. Spaldin, Eur. Phys. J. B **71**, 435 (2009).

[17] K. A. Stoerzinger, W. S. Choi, H. Jeen, H. N. Lee, and Y. Shao-Horn, The Journal of Physical Chemistry Letters **6**, 487 (2015).

[18] C. Jin-Ho, H. Yang-Su, and S. Seung-Wan, Materials letters **19**, 257 (1994).

[19] B. D. Cullity, *Introduction to Magnetic Materials* (IEEE press-Wesley, 2009), Second edition edn.

[20] B. T. Thole, P. Carra, F. Sette, and G. van der Laan, Phys. Rev. Lett. **68**, 1943 (1992).

[21] C. T. Chen, Y. U. Idzerda, H. J. Lin, N. V. Smith, G. Meigs *et al.*, Phys. Rev. Lett. **75**, 152 (1995).

[22] Y. Kim, S. Ryu, and H. Jeen, RSC Adv. **9**, 2645 (2019).

[23] P. Hohenberg and W. Kohn, Phys. Rev. **136**, B864 (1964).

[24] B. Y. Tong and L. J. Sham, Phys. Rev. **144**, 1 (1966).

[25] G. Kresse and J. Furthmuller, Phys. Rev. B **54**, 11169 (1996).

[26] J. P. Perdew, A. Ruzsinszky, G. I. Csonka, O. A. Vydrov, G. E. Scuseria *et al.*, Phys. Rev. Lett. **100**, 039902, 136406 (2008).

[27] P. E. Blochl, Phys. Rev. B **50**, 17953 (1994).

[28] H. J. Monkhorst and J. D. Pack, Phys. Rev. B **13**, 5188 (1976).

[29] G. Henkelman, B. P. Uberuaga, and H. Jónsson, The Journal of chemical physics **113**, 9901 (2000).

[30] S. Dudarev, G. Botton, S. Savrasov, C. Humphreys, and A. Sutton, Phys. Rev. B **57**, 1505 (1998).

[31] D. H. Kim, S. H. Han, Y.-M. Kang, D. Yang, and C. A. Ross, J. Alloys Compd. **692**, 545 (2017).

[32] J. Lee, E. Ahn, Y.-S. Seo, Y. Kim, T.-Y. Jeon *et al.*, Physical Review Applied **10**, 054035 (2018).

[33] G. D. Soria, P. Jenus, J. F. Marco, A. Mandziak, M. Sanchez-Arenillas *et al.*, Sci. Rep. **9**, 11777 (2019).

[34] J. Kim, S. A. Yang, Y. C. Choi, J. K. Han, K. O. Jeong *et al.*, Nano Lett. **8**, 1813 (2008).

[35] I. Fina, L. Fàbrega, E. Langenberg, X. Martí, F. Sánchez *et al.*, J. Appl. Phys. **109** (2011).

[36] M. Pal, A. Srinivas, and S. Asthana, Physica B: Condensed Matter **666**, 415127 (2023).

[37] W. Prellier, A. Biswas, M. Rajeswari, T. Venkatesan, and R. L. Greene, Appl. Phys. Lett. **75**, 397 (1999).

[38] P. R. Mickel, H. Jeen, P. Kumar, A. Biswas, and A. F. Hebard, Phys. Rev. B **93**, 9, 134205 (2016).

[39] R. Ramesh and N. A. Spaldin, Nature Mater. **6**, 21 (2007).

Table 1. Magnetic moments from SQUID and XMCD of Fe *L*-edge spectra

	M_s from M vs. H curves (μ_B/Fe)	M_{spin} from sum rule (μ_B/Fe)	$M_{orbital}$ from sum rule (μ_B/Fe)	$M_{spin} + M_{orbital}$ (μ_B/Fe)
As grown SrM	1.02	0.93	-0.03	0.90
SrM at T_a =1100°C	1.26	1.15	-0.01	1.14

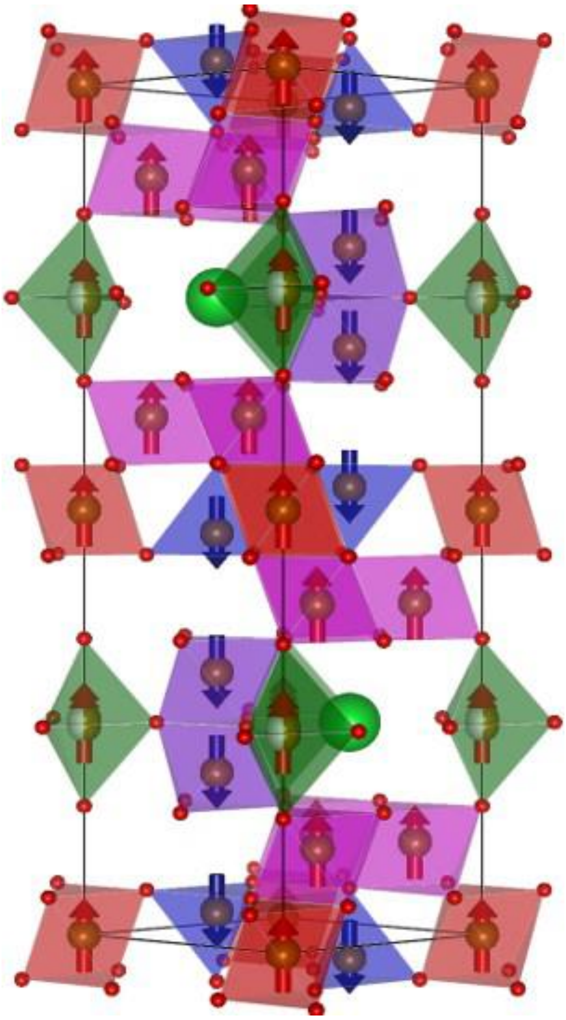

Fig. 1. Atomic structure of $SrFe_{12}O_{19}$

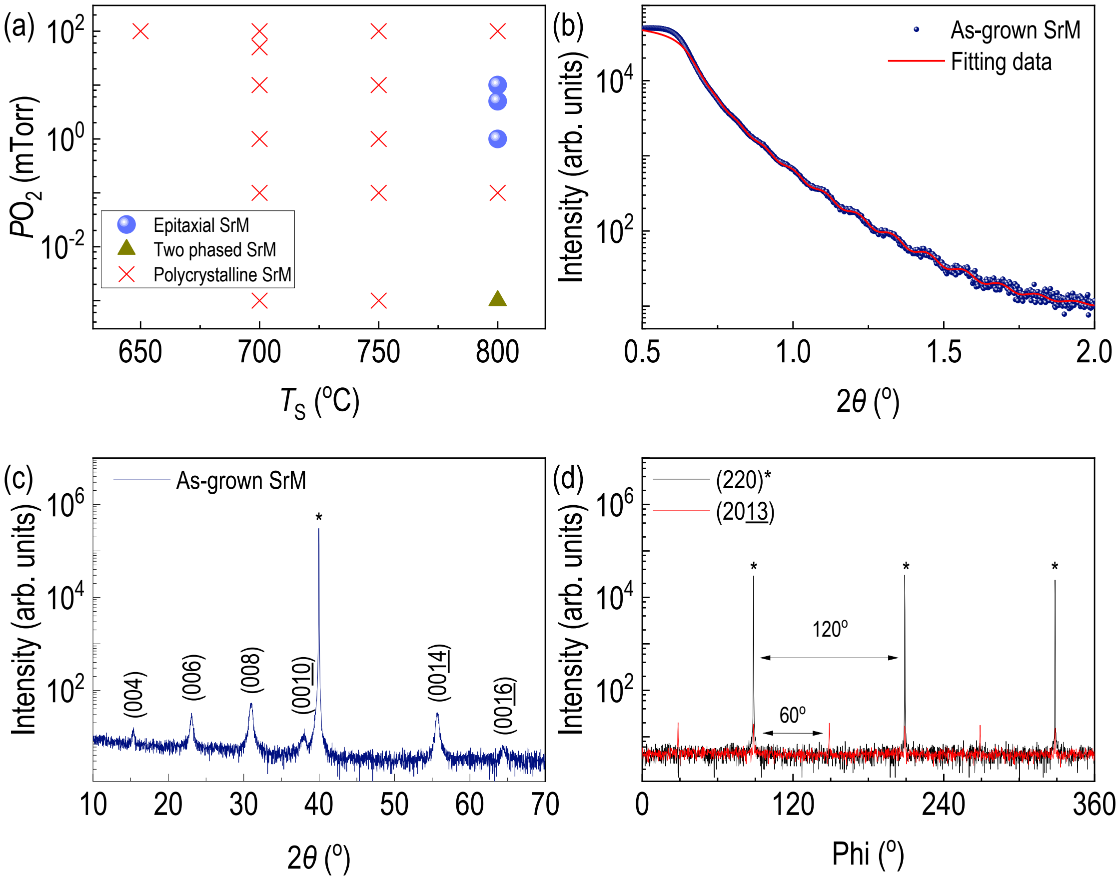

Fig. 2. (a) Growth phase diagram of SrFe$_{12}$O$_{19}$ (SrM) epitaxial thin films on (111) SrTiO$_3$. Only filled blue circles are the condition for epitaxial thin films. (b) X-ray reflectivity and its fitting of epitaxial SrM thin film grown at the optimal growth condition. (c) X-ray diffraction of the epitaxial SrM thin film on (111) SrTiO$_3$. (d) Phi scans of (220) SrTiO$_3$ and (20$\underline{13}$) SrM epitaxial thin film.

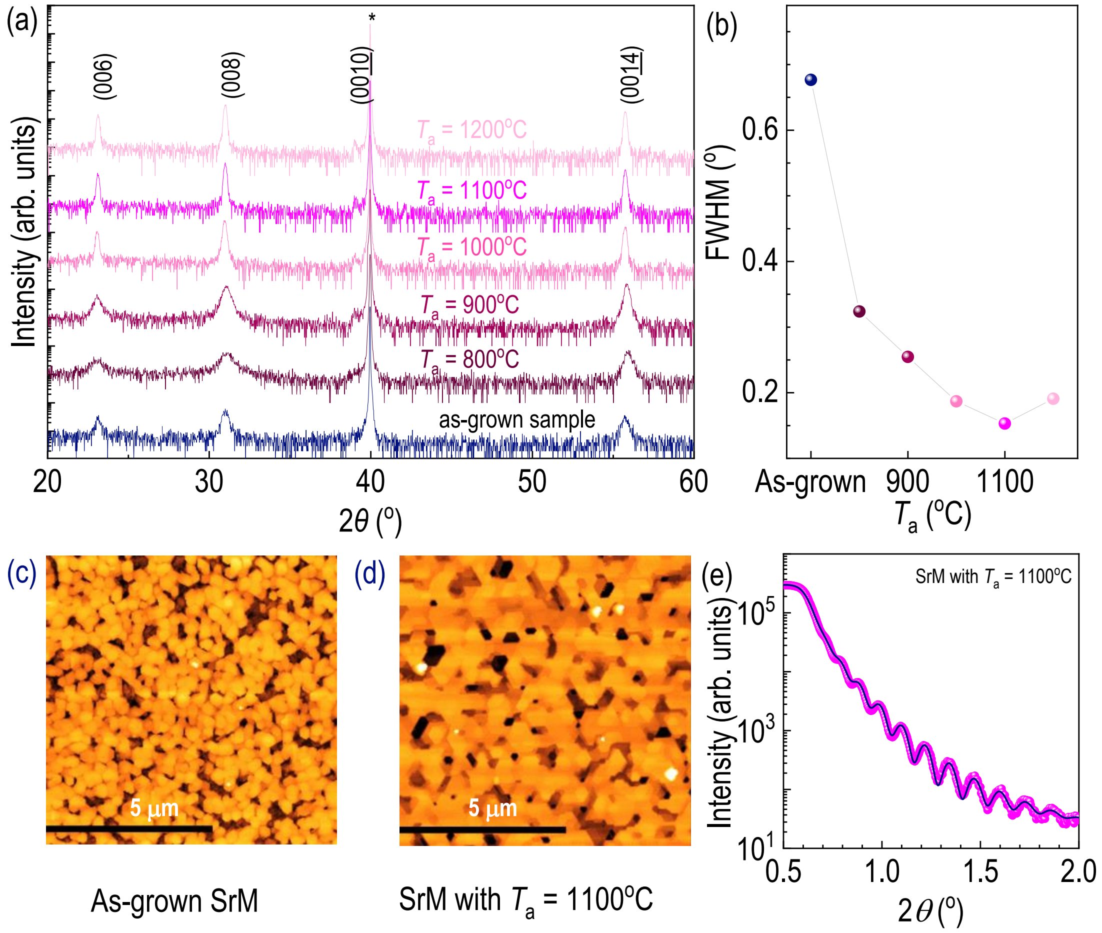

As-grown SrM

SrM with T_a = 1100°C

Fig. 3. (a) X-ray diffraction of epitaxial SrM thin films annealed at different temperatures in air. (b) Full width half maximum of rocking curves from 00<u>14</u> diffraction of SrM. Topographic images of (c) the as-grown SrM and (d) SrM annealed at 1100°C. (e) X-ray reflectivity and its fitting of SrM annealed at 1100°C.

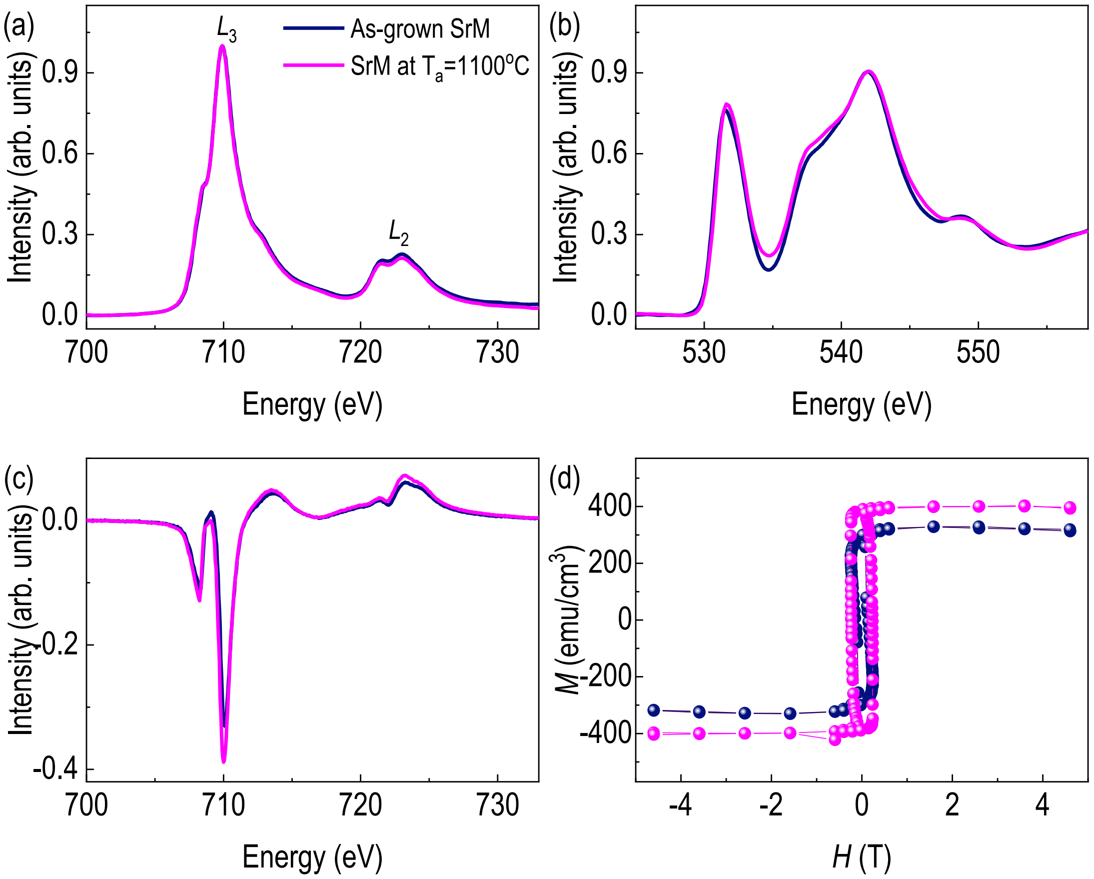

Fig. 4. X-ray absorption results are seen: (a) Fe *L*-edge spectra and (b) O *K*-edge spectra of as-grown and annealed SrM epitaxial thin films. (c) X-ray magnetic circular dichroism of as-grown and annealed SrM epitaxial thin films at 0.5 T and 300 K. (d) Magnetic hysteresis curves of as-grown and annealed SrM epitaxial thin films at room temperature, when the magnetic field is parallel to film surface normal.

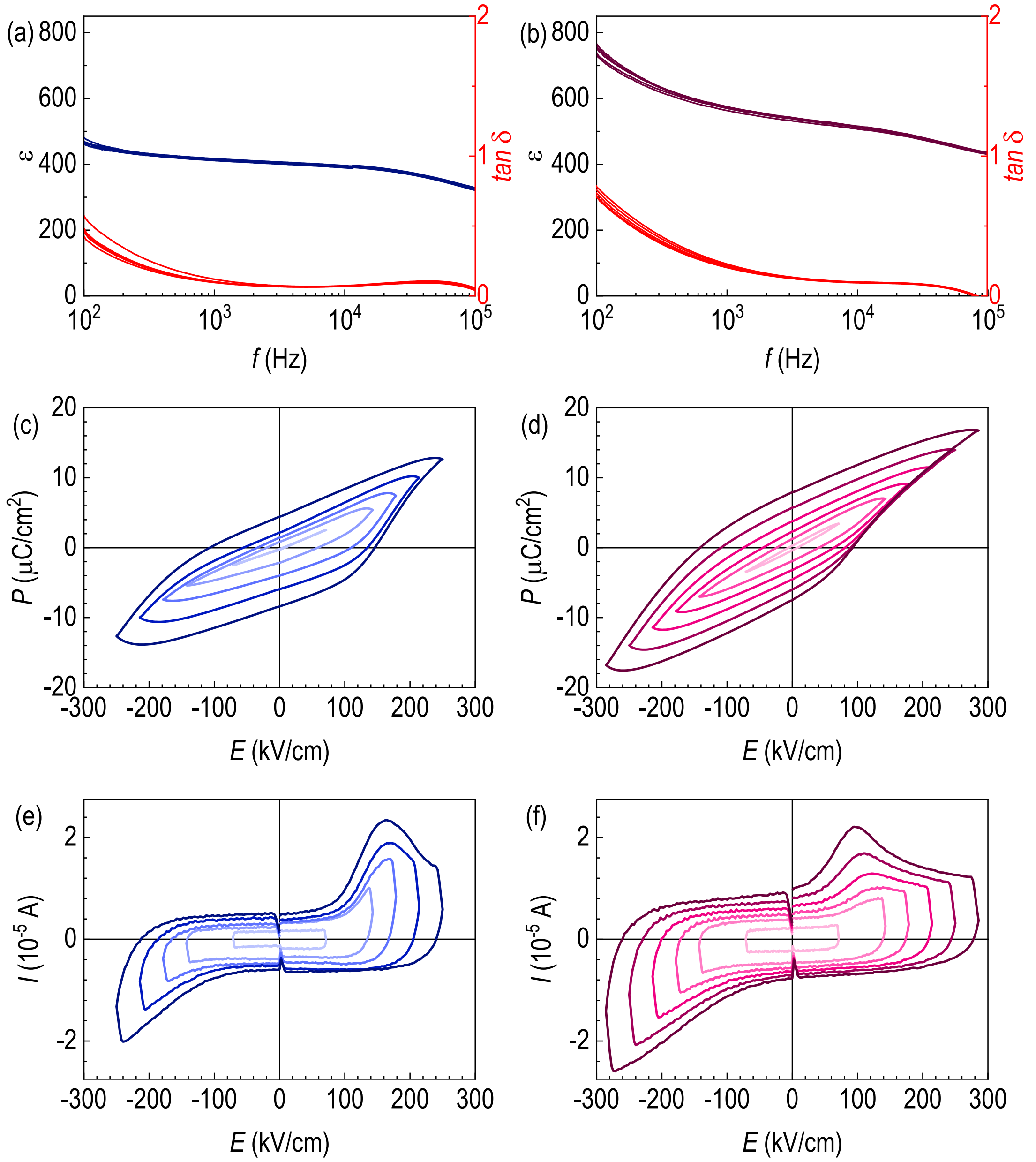

Fig. 5. Frequency-dependent dielectric constants (ε) and dissipation factors (tan δ) from (a) as-grown and (b) annealed SrM epitaxial thin films. Polarization (P) versus electric field (E) curves of (c) as-grown and (d) annealed SrM epitaxial thin films. Current (I) vs. electric field (E) curves of (e) as-grown and (f) annealed SrM epitaxial thin films. For electrical measurements, (111) 0.5% Nb doped $SrTiO_3$ substrates were used. All the measurements were taken place at room temperature.

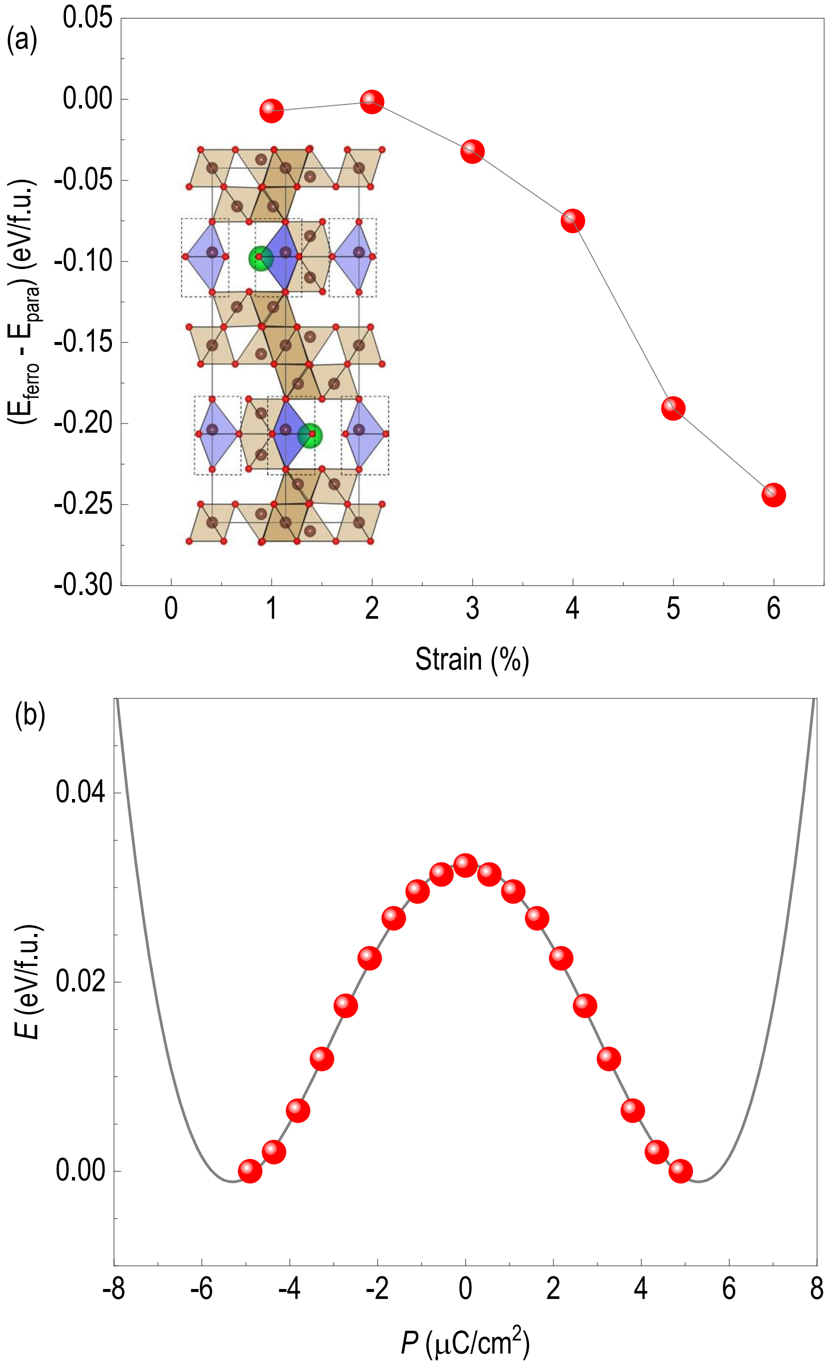

Fig. 6. (a) Energy difference between ferroelectric and paraelectric phase versus compressive strain. Inset shows atomic structure in stabilization of ferroelectric phase. (b) Energy versus polarization curve in stabilization of ferroelectric phase. Clear double well potential is built.